


Optimal Cargo Size for Active Diffusion of Biohybrid Microcarriers

Valentino Lepro^{1,2,†}, Robert Großmann^{1,†}, Setareh Sharifi Panah¹, Oliver Nagel¹,
Stefan Klumpp^{2,3}, Reinhard Lipowsky² and Carsten Beta^{1,*}

¹*Institute of Physics and Astronomy, University of Potsdam, Karl-Liebknecht Straße 24/25, 14476 Potsdam, Germany*

²*Max Planck Institute of Colloids and Interfaces, Am Mühlenberg 1, Potsdam 14476, Germany*

³*Institute for the Dynamics of Complex Systems, Georg August University of Göttingen, Friedrich-Hund-Platz 1, 37077 Göttingen, Germany*

 (Received 5 August 2021; revised 11 April 2022; accepted 1 July 2022; published 7 September 2022)

As society paves its way towards device miniaturization and precision medicine, microscale actuation and transport become increasingly prominent research fields with high impact in both technological and clinical contexts. In order to accomplish movement of micron-sized objects towards specific target sites, active biohybrid transport systems, such as motile living cells that act as smart biochemically powered microcarriers, have been suggested as an alternative to synthetic microrobots. Inspired by the motility of leukocytes, we propose the amoeboid crawling of eukaryotic cells as a promising mechanism for transport of micron-sized cargoes and present an in-depth study of this type of composite active matter. Its transport properties result from the interactions of an active element (cell) and a passive one (cargo) and reveal an optimal cargo size that enhances the locomotion of the load-carrying cells, even exceeding their motility in the absence of cargo. The experimental findings are rationalized in terms of a biohybrid active particle model that describes the emergent cell-cargo dynamics and enables us to derive the long-time diffusive transport of amoeboid microcarriers. As amoeboid locomotion is commonly observed for mammalian cells such as leukocytes, our results lay the foundations for the study of transport performance of other medically relevant cell types and for extending our findings to more advanced transport tasks in complex environments, such as tissues.

DOI: [10.1103/PhysRevApplied.18.034014](https://doi.org/10.1103/PhysRevApplied.18.034014)

The targeted delivery of micron-sized objects, such as drug-releasing microparticles or nanoelectronic biosensors, is one of the prime challenges in modern medical technology. Ideally, future solutions will rely on mechanisms of self-propulsion, allowing micron-sized cargoes to actively navigate through complex and crowded environments such as human tissue [1,2]. To achieve this goal, much effort has been devoted to the design of bioinspired synthetic microrobots [3–10]. However, several technical difficulties limit this approach, such as questions of power supply, biocompatibility, and efficient steering, especially in complex environments [1,11–18]. Rather than reinventing nature’s sophisticated machines, an alternative paradigm to address this challenge is to take advantage of them directly: by loading microcargoes onto motile cells, their innate migratory abilities can be exploited to achieve microtransport in a biohybrid approach [1,12,16,19–21]. While this principle has been successfully demonstrated with the help of self-propelled bacterial swimmers, the

physical properties and, particularly, the transport capacities of the most common modes of eukaryotic locomotion, such as amoeboid crawling of leukocytes during an inflammatory response [22–24], have remained mostly unexplored and were only recently exemplified in a few cases [25–27].

At a theoretical level, the physical properties of actively moving entities, nowadays referred to as active matter, is one of the most rapidly evolving subfields of physics that connects fundamental questions of nonequilibrium thermodynamics and statistical mechanics with current challenges and open questions in our understanding of complex biological systems [28–30]. While early active matter research has mostly been driven by fundamental theoretical questions [29,31,32], the field is now increasingly focusing on specific experimental model systems, studying, for example, the formation of emergent patterns in motor-driven assemblies of cytoskeletal filaments [33], the movement of bacterial swimmers [34], or collective motion [35]. However, the potential of cargo-carrying active particles to fulfill transport tasks has been largely ignored and has only recently been discussed in modeling studies and for synthetic systems [36,37].

*beta@uni-potsdam.de

†These two authors contributed equally.

In this work, we combine live cell experiments with theoretical modeling to study the fundamental principles of active biohybrid transport driven by adherent eukaryotic cells. The active biohybrid is composed of an amoeboid cell as an active element and a polystyrene bead ranging in diameter from 10 to 100 μm as cargo. We rely on cells of the social amoeba *Dictyostelium discoideum* (*D. discoideum*), a well-established model organism for actin-driven motility of eukaryotic cells that shares many similarities with neutrophils [38,39]. Given the highly non-specific adhesion of our model organism [40], the binding of microcargo to the cell membrane does not require any surface functionalization, whereas this may be required for specific applications with other cell types. The physical link between cargo and carrier is established spontaneously; as a cell gets in contact with a particle, the cargo adheres to the cell membrane and is then subjected to forces exerted by the cell. We first present an experimental study of the emergent short-time dynamics of this composite cell-cargo system that is driven by the mechanoresponsiveness of the amoeboid cells. This analysis then serves as a basis to establish a model description for biohybrid microcarriers that allows us to infer how the cell-cargo interactions shape the diffusive long-time transport in an isotropic environment. Our study reveals a nonmonotonic dependence of the diffusivity on cargo size, thus demonstrating the existence of an optimal cargo size that maximizes the transport efficiency, even exceeding the spreading of single cells in the absence of cargo. Note that, at a qualitative level, directed biohybrid transport by *D. discoideum* cells has also been demonstrated, relying on the chemotactic capacity of this cell type [41]. As a proof of concept, we show experiments of chemotactic motion in a chemical gradient, revealing that key features of the motion pattern in the absence of external cues are preserved during chemotactic motion. This suggests that our analysis of diffusive spreading of amoeboid microcarriers can be extended in the future to also study the directional transport of microcargoes.

I. CELL-CARGO SYSTEM SHOWS MULTIPLE TRANSPORT PHASES

A general view of the biohybrid cell-cargo system, referred to hereafter as *cellular truck* or *truck*, is given in Fig. 1(a) along with a schematic in the inset, depicting its typical conformation: the particle resides on top of the cell, typically towards its rear edge, while the cell moves forward, thereby pulling the cargo (see the Supplemental Material for movies [42]). Tracking of the colloid position reveals that the mean-squared displacements of the cargo particle, shown in Fig. 1(b), is nonmonotonic in particle size: notably, for small cargo particles, the transport efficiency increases with increasing cargo size until an optimal, intermediate cargo diameter is reached, which

maximizes the transport efficiency of the cellular truck. To elucidate the mechanism that leads to these counterintuitive transport properties of cellular trucks is one of the central aims of this study.

We perform dual-color fluorescence imaging experiments, where the motions of the cell and cargo are resolved, while at the same time visualising the polarization of the cytoskeleton. For this, we use a *D. discoideum* cell line that expresses fluorescent labels of *F*-actin and myosin II, known to localize at the leading edge and at the rear of a polarized cell, respectively [43,44]. In the following, we denote cell polarization by the unit vector \mathbf{e}_p , and the centers of the cell and cargo by the two-dimensional position vectors \mathbf{r} and \mathbf{R} , respectively, defined in the focal plane of imaging, which is parallel to the substrate surface (cf. the Appendix). This experimental setting enables us to study the cargo dynamics with respect to the cell in terms of the distance vector

$$\mathbf{l}(t) = \mathbf{R}(t) - \mathbf{r}(t); \quad (1)$$

cf. Fig. 1 for an illustration.

From our microscopy recordings, we identify two distinct transport phases that are separated by polarity bursts and robustly emerge for all tested particle sizes; cf. Fig. 1(c)–1(e). During *resting phases*, the cell and particle move around each other, keeping their distance $l(t) = |\mathbf{l}(t)|$ approximately constant without significant net displacement of the whole truck. In this phase, the cell shows no or only short-lived cytoskeletal polarization. Trucks can dwell in the resting phase for up to several minutes. In addition, we observe intermittent *polarity bursts*, where the cell suddenly reorients and polarizes towards the cargo, crawling underneath and at the same time pulling the cargo towards its newly defined rear. This process usually takes a few minutes; we call its rate of occurrence λ (polarization rate). After such transitions, a *motile phase* follows, where cell polarization is maintained, causing the cell to keep moving and pulling the cargo forward. This phase is associated with significant displacement of the cellular truck. Once the cell spontaneously depolarizes, typically after a polarity lifetime $\tau_p = \sigma^{-1}$ of a few minutes, the persistent run ends and the truck returns to the resting phase, waiting for another polarization event to be triggered. The cell may also repolarize towards the cargo while being in the motile phase; in such cases, the truck ends its current run and directly enters the next polarity burst; see Fig. 1(e) for a schematic representation of the sequence of cell polarization and depolarization together with the corresponding rates of occurrence. With respect to the cell, we may thus distinguish two states s , an isotropic ($s = 1$) and a polarized state ($s = 2$), where the latter incorporates both, the polarity burst and the subsequent motile phase.

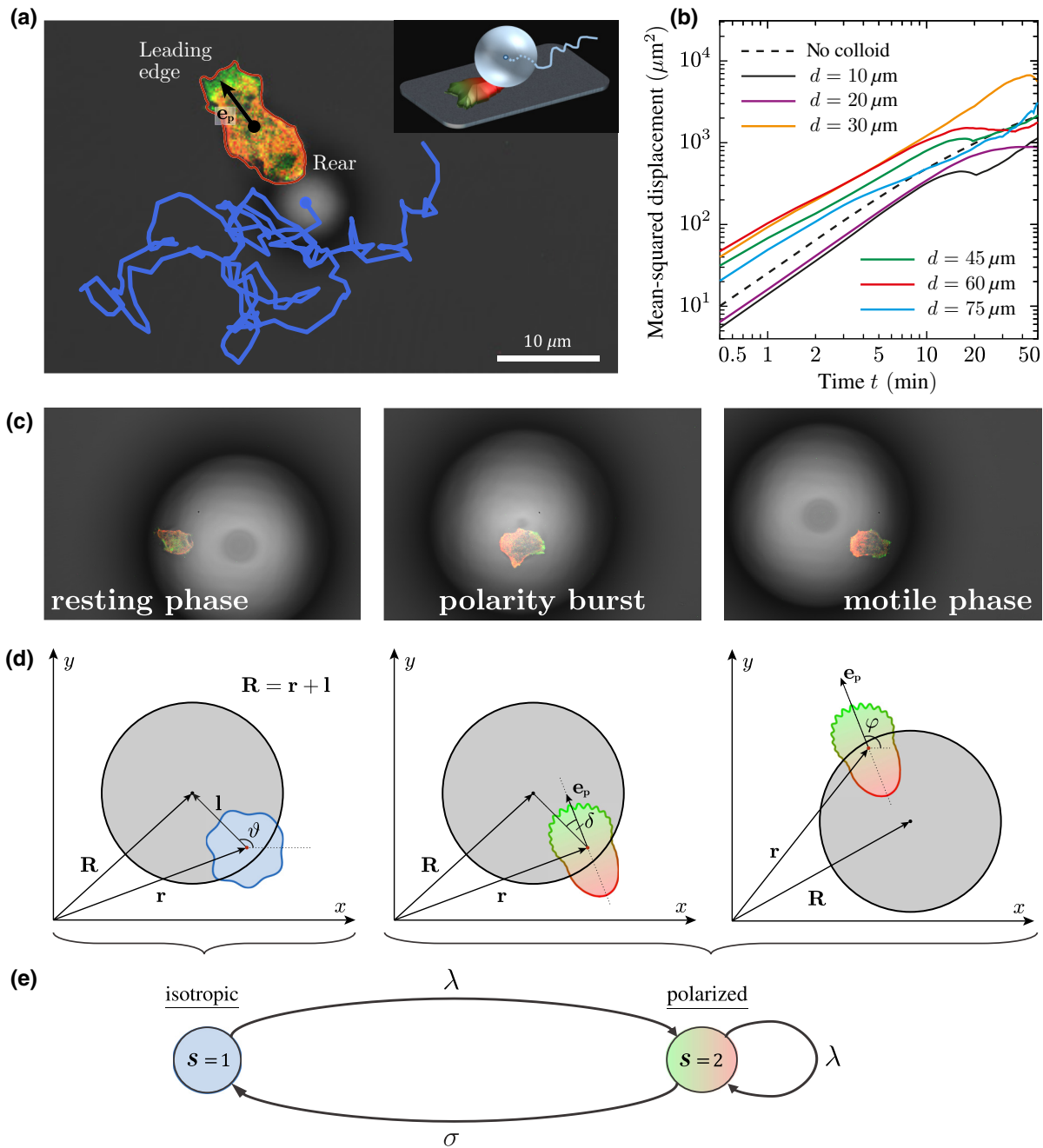


FIG. 1. Phenomenology of the cell-cargo truck and its dynamics. Panel (a) shows the cell and cargo as observed experimentally together with an exemplary trajectory of the cargo. The snapshot shows a polarized cell as indicated by a black arrow, where F -actin is color coded in green and myosin II in red. An illustration of the three-dimensional spatial configuration of the cell and cargo is presented in the inset. The ensemble averages of the time-averaged mean-squared displacements (MSDs) of cargoes of fixed size, transported by the cell, are shown in panel (b); note that less data points are typically available for the averaging procedure for large time lags, which is the reason why the curves become noisy in the long-time limit [cf. Appendix A 5 for additional technical details, particularly Eqs. (A5)–(A10)]. Notably, the transport efficiency is nonmonotonic in particle size and reaches a maximum for intermediate sizes. Moreover, the MSD of cells that are loaded with a particle can exceed the MSD of unloaded cells [dashed line in panel (b)]. The three panels in (c) indicate the typical phases of cellular truck dynamics. In (d), key geometric quantities are introduced: the positions of cell \mathbf{r} and cargo \mathbf{R} , the distance vector $\mathbf{l} = \mathbf{R} - \mathbf{r}$ with its polar angle ϑ , the cell polarization vector \mathbf{e}_p along with the cell polarization angle φ , and the angle δ indicating the direction of initial cell polarization compared to the cell-cargo axis, given by the distance vector \mathbf{l} . A depolarized cell in the left panel is shown in blue; polarized cells are represented by a red-green gradient. The sequence of cell polarization and depolarization is illustrated in panel (e) together with the corresponding rates of occurrence (λ and σ , respectively): the polarized state ($s = 2$) in panel (e) is highlighted in red and green, resembling the nonuniform distribution of F -actin and myosin II within the cell in this state. For movies, see the Supplemental Material [42].

II. CELL-CARGO DISTANCE DISPLAYS RECURRENT DYNAMICS

The cyclic change between the three transport states (resting phase, polarity burst and motile phase) gives rise to a recurrent yet stochastic dynamics for the distance $l(t) = |\mathbf{I}(t)|$ between the cell and particle, as illustrated for three different particle sizes in Fig. 2(a). The distance fluctuates around a preferred value l_0 , interrupted by repeated abrupt decays that correspond to the polarity-induced crossing events, when the cell moves underneath the particle, shifting it towards its other side. The value of the preferred distance l_0 increases with increasing cargo size. Histograms of the time series of the distance consistently display a peaked distribution with a negative skew due to the crossing events. Note that we also observe pronounced differences in the polarization rate λ for different cargo sizes: the average time interval $\tau = \lambda^{-1}$ between polarity bursts increases with the particle diameter d .

A more detailed look at the relative cell-cargo dynamics is presented in Fig. 2(b). Here, the frame of reference is aligned with the center of the cell $\mathbf{r}(t)$, and the relative cargo trajectory $\mathbf{I}(t) = \mathbf{R}(t) - \mathbf{r}(t)$ is plotted using a color scale to encode time. Typically, the cell pulls the cargo randomly around itself, keeping on average a characteristic distance l_0 . From time to time, however, the cell moves towards the particle center, crossing to the other side. The larger the particle, the more prominent this motion pattern is; see the trajectories of the relative motion of cells loaded with 45 and 75 μm particles.

To obtain a more quantitative representation of the cell-cargo dynamics, we generate recurrence plots [45,46] from the time evolution of the distance vector $\mathbf{I}(t)$. Recurrence plots graphically represent to which degree a dynamical system revisits similar areas in phase space at times t_i and t_j by means of a matrix $I(t_i, t_j)$. In Fig. 2(c), examples of recurrence plots are shown, where $I(t_i, t_j)$ is color coded; they correspond to the relative motion of the three examples shown in panels (a) and (b). These recurrence plots compare the vectors $\mathbf{I}(t)$ pointing from the cell to the center of the colloid at different times. Consequently, the recurrence parameter is small whenever the vector \mathbf{I} returns to a prior location, $\mathbf{I}(t_i) \simeq \mathbf{I}(t_j)$, and is large, in contrast, if $\mathbf{I}(t_i)$ differs from $\mathbf{I}(t_j)$. Blue patches in the recurrence plots thus indicate phases where the colloid stays at a similar position with respect to the cell, whereas sudden changes from blue to yellow point to transitions, i.e., polarity bursts during which the cell suddenly pulls the cargo to another location. The recurrence plots display a distinctive checkerboard pattern: in our context, patches correspond to resting or motile phases, separated by sharp boundaries that are related to randomly occurring polarity bursts. The checkerboard structure becomes increasingly pronounced for larger cargoes. Furthermore, the polarization rate decreases for larger particles, which is reflected

by larger patches in the recurrence plots. Taken together, the analysis of recurrence plots suggests an intermittent relative dynamics, where dwelling at a certain preferred cell-particle distance $l(t) \approx l_0$ alternates with stochastically occurring sudden episodes of relative motion, during which the cell polarizes towards the cargo, moves underneath it, and the cargo is simultaneously pulled from one side of the cell to the other.

Additionally, we calculate population-averaged histograms of the distance $l(t)$ by binning several time series for a given particle size [see Fig. 3(a)]. The emerging ensemble-averaged distributions retain a peaked shape as for the single truck. With increasing particle diameter d , the peak position shifts towards larger values and the histograms become wider. Given these distributions, we infer an effective cell-cargo interaction potential $\Phi(l)$ in the vicinity of the peak by Boltzmann inversion of the histogram $p(l)$ via

$$p(l) \sim e^{-\Phi(l)}, \quad (2)$$

relating the probability distribution of a physical quantity to an effective energy landscape [47]. As shown in Fig. 3(b), the inferred potentials are harmonic close to the peak position. Together with the recurrence plot analysis, this suggests that the cell-cargo dynamics can be described as an elastic interaction, recurrently perturbed by polarity bursts in the course of which the cell moves underneath the cargo, pulling it onto its other side.

III. AN ACTIVE PARTICLE MODEL OF CELLULAR TRUCK DYNAMICS

Based on the experimental observations, we propose a phenomenological model that mimics the dynamics of a cellular truck. The cell is the actual active element—any displacement of the cell and particle results from active forces exerted by the cell onto the cargo or the substrate. In contrast, thermal diffusion of the cargo is negligible for the particle sizes considered. The model relies on the observation that the cell can adopt two states at random: an *isotropic state* ($s = 1$) and a *polarized state* ($s = 2$); see Fig. 1.

In the isotropic state ($s = 1$), the cell moves diffusively with an effective diffusion coefficient D_i . The particle, adherent to the cell, is pulled around it randomly; the cell-cargo distance fluctuates around a characteristic value l_0 that depends on the size of the particle. The key mechanism that determines the dynamics of the truck is the cell's tendency to polarize towards the cargo. In the polarized state ($s = 2$), the cell exerts net forces on its environment, thereby (i) enabling persistent motion at a nonvanishing speed v_0 that we assume to be constant for simplicity and (ii) pulling the particle onto its back with respect to the cell

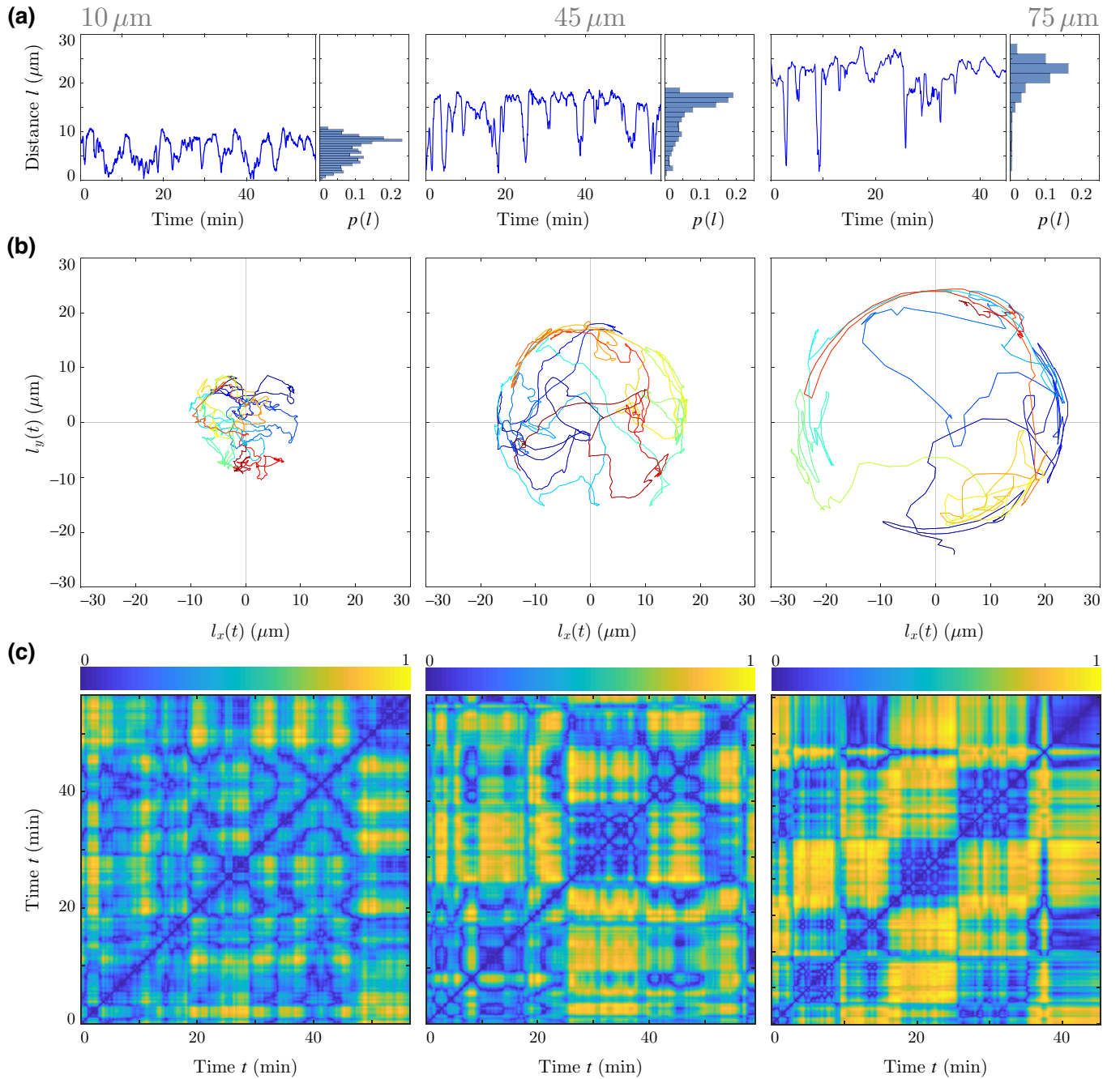


FIG. 2. Relative dynamics of the cell and cargo. In (a), time series of the distance $l(t) = |\mathbf{R}(t) - \mathbf{r}(t)|$ between the cell and cargo are shown together with the corresponding histograms. The dynamics of the cargo in the frame of reference of the cell is plotted in (b), where time is color coded from blue (beginning) to red (end). Panels (c) display color-coded recurrence plots $I(t_i, t_j) = [\Delta_{ij} - \min_{ij}(\Delta_{ij})] / [\max_{ij}(\Delta_{ij}) - \min_{ij}(\Delta_{ij})]$, where $\Delta_{ij} = |\mathbf{l}(t_j) - \mathbf{l}(t_i)|$ and $\mathbf{l}(t) = \mathbf{R}(t) - \mathbf{r}(t)$; $\min_{ij}(\Delta_{ij})$ and $\max_{ij}(\Delta_{ij})$ denote the minimal and maximal entries in one specific matrix Δ_{ij} , respectively. Since the colloid and cell are constantly in contact, the dynamics of $\mathbf{l}(t)$ is bounded to a confined domain [cf. panel (b)]. One can therefore normalize the matrix Δ_{ij} to obtain $I(t_i, t_j)$, such that minimal values are set to zero and maximal values equal one. The checkerboard structure of these plots suggests a recurrent dynamics; the increasing patch size is due to fewer transitions, i.e., a decrease of the cell polarization rate with colloid size (cf. main text for interpretation). Columns correspond to three different particle diameters: $d = 10 \mu\text{m}$ (left), $d = 45 \mu\text{m}$ (middle), and $d = 75 \mu\text{m}$ (right).

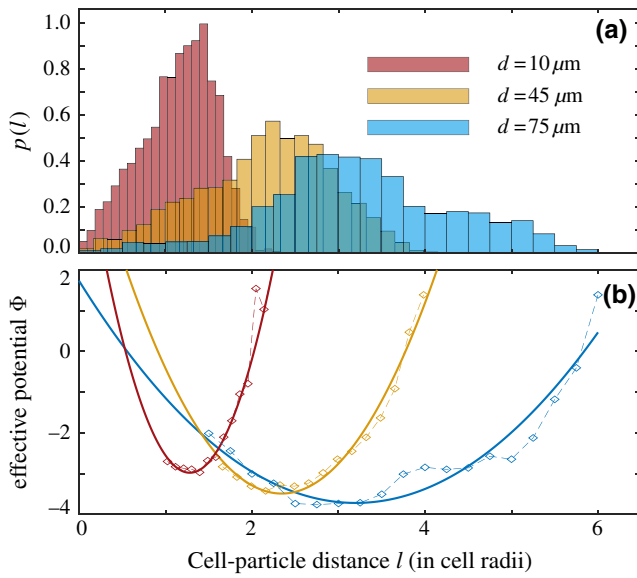


FIG. 3. Population-averaged histogram of cell-cargo distance and their effective interaction potential. In panel (a), population averaged histograms of the cell-particle distance, measured in multiples of an effective cell radius r_c to account for cell size variability, are shown (cf. the Appendix for calculation of r_c). Population averages are taken over ten independent experimental realizations for each cargo size. Based on these histograms, effective potentials are inferred [panel (b)] via the Boltzmann formula $p(l) \sim e^{-\Phi(l)}$. The peak of the histogram relates to an effective harmonic interaction potential; fits using quadratic functions are shown by solid lines in (b). Only those data points that are included into the fit are plotted; for $l \rightarrow 0$, the potential is expected to be anharmonic due to the polarization dynamics [Fig. 1(c)], which is why those data points are excluded from fitting.

polarization vector

$$\mathbf{e}_p[\varphi(t)] = \begin{pmatrix} \cos \varphi(t) \\ \sin \varphi(t) \end{pmatrix}, \quad (3)$$

which is parametrized in terms of the polarization angle φ and defined to have unit length (cf. Fig. 1).

Mathematically, the spatial dynamics of the cell's center $\mathbf{r}(t)$ is described by the equations

$$\dot{\mathbf{r}}(t) = v(s)\mathbf{e}_p[\varphi(t)] + \sqrt{2D(s)}\boldsymbol{\xi}_r(t), \quad (4a)$$

$$\dot{\varphi}(t) = \sqrt{2D_\varphi}\xi_\varphi(t). \quad (4b)$$

The speed $v(s)$ and the coefficient $D(s)$ of Brownian diffusion (Wiener process) are state dependent: $v(1) = 0$ for state $s = 1$, whereas $v(2) = v_0$ in the polarized state; furthermore, we denote $D(1) = D_i$ and $D(2) = D_p$, respectively. The terms $\boldsymbol{\xi}_r$ and ξ_φ represent independent Gaussian white noise processes with zero mean and temporal δ -correlations [48].

The position of the particle $\mathbf{R}(t)$, adherent to the cell, is described by a linear interaction term (cf. Fig. 3) and unbiased Gaussian white noise $\boldsymbol{\xi}_R$ that accounts for non-thermal displacement due to undirected forces exerted on the particle by the cell:

$$\dot{\mathbf{R}}(t) = -\alpha[\mathbf{R} - \mathbf{R}_0(s)] + \sqrt{2D_R}\boldsymbol{\xi}_R(t). \quad (5)$$

In the passive state ($s = 1$), the distance $l = |\mathbf{R} - \mathbf{r}|$ between the cell and particle fluctuates around a characteristic value l_0 , while the particle can circle around the cell. The ratio D_R/α of the noise intensity D_R and the spring constant α determines the strength of fluctuations of l and, thereby, the width of the histogram of the cell-particle distance l ; $1/\alpha$ is a characteristic timescale of the cell-particle dynamics [Eq. (5)]. In the polarized state, the particle moves to the back of the cell with respect to its polarization \mathbf{e}_p . This is modeled by a state-dependent minimum position $\mathbf{R}_0(s)$ of the interaction potential in Eq. (5):

$$\mathbf{R}_0(s) = \mathbf{r} + l_0 \cdot \begin{cases} \mathbf{l}/|\mathbf{l}|, & s = 1, \\ -\mathbf{e}_p[\varphi], & s = 2. \end{cases} \quad (6)$$

Lastly, we describe transitions between the isotropic and polarized states ($s = 1$ and $s = 2$, respectively) as Poisson processes with transition rates $\{\lambda, \sigma\}$; see Figs. 1(d) and 1(e). In the isotropic state, the cell does not exhibit any polarization; cf. Eq. (4a) with $v(1) = 0$. At each polarity burst, occurring at a rate λ , vector \mathbf{e}_p is initialized anew and now affects the dynamics of the cell as $v(2) = v_0$ in Eq. (4a). Because of the mechanical stimulus of the cargo, the cell tends to polarize along the cell-cargo axis $\mathbf{l} = l(\cos \vartheta, \sin \vartheta)$ on average, i.e., towards the current position of the cargo, plus some angular variability δ . A polarity burst is therefore mathematically described by resetting the polarization angle $\varphi \rightarrow \vartheta + \delta$, so that the polarization vector becomes

$$\mathbf{e}_p \rightarrow \begin{pmatrix} \cos[\vartheta + \delta] \\ \sin[\vartheta + \delta] \end{pmatrix}. \quad (7)$$

The random angle δ is drawn from a narrow Gaussian distribution centered at zero. In this way, variability in the orientation of cell polarization upon polarity bursts is taken into account.

The model reproduces all essential features of the experimentally observed dynamics of the cell-cargo motion as illustrated in Fig. 4; in addition, a comparison (experiment versus numerical simulations) of the scaling regimes of the mean-squared displacement of the cargo transported by a cell is discussed in the Supplemental Material [42]. The time series of the cell-cargo distance [Fig. 4(a)] shows an intermittent dynamics with pronounced, recurring downward spikes perturbing the fluctuations around

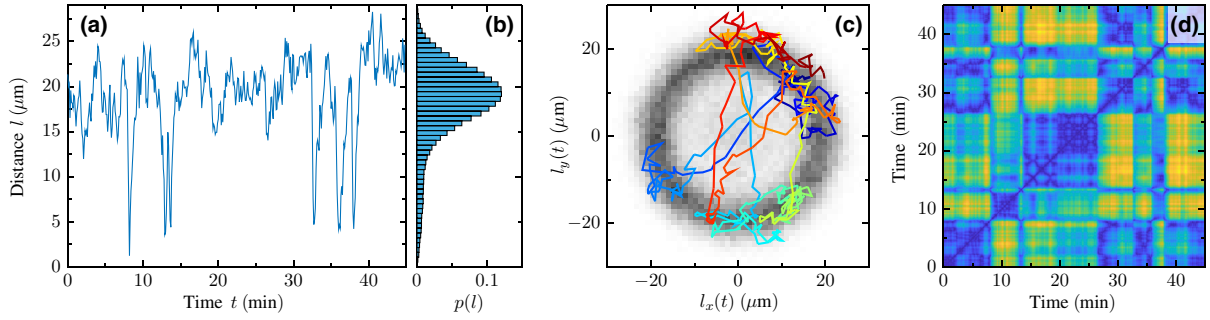


FIG. 4. Predictions of the active particle model for the cell-cargo dynamics. The representation of simulation results corresponds to the experimental results displayed in Fig. 2: (a) time series of the distance of the centers of mass of the cell and cargo together with the corresponding histogram [panel (b)]; (c) trajectory of the cargo in the frame of reference of the cell, where time is color coded from blue (beginning) to red (end); in the background, the two-dimensional histogram of the distance vector \mathbf{I} , drawn from a long simulation run, is shown in grayscale—it indicates the rotational symmetry (isotropy) of the colloid dynamics around the cell; (d) recurrence plot $I(t_i, t_j)$ of the distance vector $\mathbf{I}(t) = \mathbf{R}(t) - \mathbf{r}(t)$ (cf. Fig. 2). All features of the experimentally observed cellular truck dynamics are qualitatively reproduced by the model. Parameter values are $\sigma = 0.1 \text{ min}^{-1}$, $\lambda = 0.139 \text{ min}^{-1}$, $\alpha = 2 \text{ min}^{-1}$, $D_R = 13 \text{ } \mu\text{m}^2/\text{min}$, $l_0 = 18 \text{ } \mu\text{m}$, $v_0 = 6 \text{ } \mu\text{m}/\text{min}$, $D_\varphi = 0.1 \text{ min}^{-1}$, $D_i = 1 \text{ } \mu\text{m}^2/\text{min}$, $D_p = 1 \text{ } \mu\text{m}^2/\text{min}$, $\delta \sim \mathcal{N}(0, 0.2)$, numerical time step $\Delta t = 0.01 \text{ min}$ (stochastic Euler method [48]).

the characteristic distance l_0 . Spikes correspond to polarization events during which the cell pulls the cargo from its leading to its trailing edge. The associated histogram [Fig. 4(b)] of the cell-cargo distance reveals a pronounced peak and a characteristic asymmetry, similar to the experimentally observed histograms (cf. Fig. 2). Cargo trajectories in the frame of reference of the cell extracted from simulations structurally resemble the experimentally observed trajectories [Fig. 4(c)], and the corresponding recurrence plots show a checkerboard structure, consistent with the experimental results; see Fig. 4(d).

IV. MODEL SIMULATIONS OF LONG-TIME DYNAMICS PREDICT AN OPTIMAL CARGO SIZE THAT MAXIMIZES TRUCK DIFFUSIVITY

Polarity bursts followed by persistent motion are the key dynamical feature that drives the net motion of a cellular truck. At the modeling level, the polarization rate λ is thus the central parameter that controls the long-time diffusion constant \mathcal{D} of the truck. Experimentally, we observed that λ decreases with cargo diameter d ; see Figs. 2 and 5(a). In experiments, the rate λ is thus indirectly controlled by choosing the cargo diameter. Together, the two dependencies $\lambda(d)$ and $\mathcal{D}(\lambda)$ determine the pivotal role of cell-cargo interaction for cargo transport.

Simulations of the cellular truck model [Eqs. (3)–(7)] enable us to predict the long-time dynamics of the truck as a whole, quantified based on the mean-squared displacement. The model predicts a nonmonotonic dependence of the diffusion coefficient \mathcal{D} on the polarization rate λ . This is illustrated in Fig. 5(b), where the diffusion coefficient, numerically calculated for different polarization rates λ , is plotted together with an analytical estimate of

$\mathcal{D}(\lambda)$ derived via a systematic mode reduction of the master equation corresponding to the particle-based Langevin model (mathematical details of the derivation are provided as Supplemental Material [42]). Both, numerical simulations and analytical estimates predict a markedly peaked functional dependence $\mathcal{D}(\lambda)$. The maximum is located around values of λ comparable to the depolarization rate σ ,

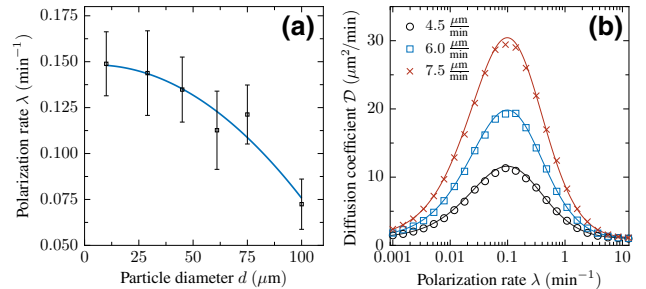


FIG. 5. Long-time transport properties of the cell-cargo truck. (a) Dependence of the polarization rate λ on the particle diameter inferred from experimental data (cf. the Appendix), along with a parabolic fit indicating a monotonous decay. (b) Nonmonotonic dependence of the long-time diffusion coefficient on the polarization rate λ as predicted by the active particle model. Simulations (points) and the theoretical prediction (lines), cf. the Appendix, are in full agreement. The comparison is shown for three different speed values: $v_0 = 4.5 \text{ } \mu\text{m}/\text{min}$ (black circles), $v_0 = 6 \text{ } \mu\text{m}/\text{min}$ (blue squares), and $v_0 = 7.5 \text{ } \mu\text{m}/\text{min}$ (red crosses). Other parameters are identical to Fig. 4. The monotonic decay of the polarization rate as a function of the particle diameter together with the nonmonotonic scaling of the long-time diffusion coefficient of the truck as a function of the polarization rate suggest the existence of an optimal cargo diameter that maximizes the transport capabilities of the cellular truck.

which is defined as the inverse of the lifetime of the polarized state of the cell, encoding the experimentally observed persistence in cell motility during the motile phase (cf. Fig. 1). As discussed previously, most of the displacement of the cellular truck is observed during this phase. Since the polarization rate decreases monotonically with increasing particle diameter d and the depolarization rate σ is independent of d as it is inherent to the cell, the model thus predicts a nonmonotonic dependence of the diffusion coefficient on cargo size. In short, an optimal cargo size maximizes the transport efficiency of a cellular truck.

V. SCALING ARGUMENTS AND EXPERIMENTAL DATA CONFIRM AN OPTIMAL CARGO SIZE

To comprehend the physical mechanism behind the nonmonotonic relation between cargo size and truck diffusivity and in order to provide an intuition for the peak location, we present a simple scaling argument. There are two relevant timescales in this setting: first, the dwelling time $\tau = \lambda^{-1}$ that is set by the polarization rate λ and, second, the lifetime of the polarized state $\tau_p = \sigma^{-1}$. Let us approximate the trajectory of a truck as a sequence of independent, persistent runs of length l_{run} , interrupted by reorientations (polarization events that occur at a rate λ). To lowest order, we may estimate the diffusion coefficient of the truck as $\mathcal{D} \sim l_{\text{run}}^2/\tau$, where $l_{\text{run}} \approx v_0 \tau_{\text{run}}$ is the typical run length between two reorientation events and τ_{run} is the time for which a truck is actually running. The run time τ_{run} depends on the lifetime of the polarized state τ_p and the dwelling time τ . If the lifetime of cell polarization is shorter than the typical time at which reorientations occur, i.e., $\tau_p \ll \tau$, the run time equals the cell polarization time ($\tau_{\text{run}} = \tau_p$) such that $l_{\text{run}} = v_0 \tau_p$ and, consequently, $\mathcal{D} \sim \tau^{-1}$. However, in the opposite limit ($\tau_p \gg \tau$), runs are cut short because reorientations may be spontaneously triggered during a run. Accordingly, the run time is determined by the inverse reorientation rate ($\tau_{\text{run}} = \tau$), thus implying the scaling $\mathcal{D} \sim \tau$. Therefore, the following nonmonotonic dependence of the diffusion coefficient on τ is expected:

$$\mathcal{D} \sim \begin{cases} \tau, & \tau \ll \tau_p, \\ \tau^{-1}, & \tau \gg \tau_p. \end{cases} \quad (8)$$

While the lifetime of cell polarization τ_p is an intrinsic feature of the cell, the polarization rate λ depends on cargo size, as it decreases monotonically with the particle diameter according to our experimental findings [Fig. 5(a)]. Therefore, an optimal particle size for cell-driven transport is expected, in line with the predictions of model simulations presented above: small particles cause frequent reorientations, thus stopping runs too early; on the other hand, large particles let the cell-cargo system dwell in a nonpolar, nonmotile state, which is inefficient for transport.

This nonmonotonic scaling of the diffusion coefficient with particle size represents our main insight into cell-driven cargo transport.

The theoretical prediction of a nonmonotonic trend in the transport efficiency as a function of cargo diameter also yields an explanation of our initial experimental observations displayed in Fig. 1(b). Notably, cellular trucks loaded with particles of intermediate size spread faster than unloaded cells. This counterintuitive observation supports our modeling hypothesis that symmetry breaking induced by the mechanical cell-cargo interaction triggers repeated bursts of cell polarization, thereby promoting motility of the cellular truck as a whole. Note also that simulations of our model returned realistic values for the diffusion coefficient \mathcal{D} , predicting its maximum if polarization and depolarization rate are comparable ($\lambda \simeq \sigma$).

VI. CHEMOATTRACTANT CONCENTRATION GRADIENTS ENABLE DIRECTIONAL PARTICLE TRANSPORT BY CELLS

As a proof of concept, we perform experiments in gradients of cAMP (cyclic adenosine monophosphate), which acts as a chemoattractant for *D. discoideum* cells. In the Supplemental Material [42], we provide three exemplary movies that clearly show directed transport of microparticles by cells that persistently move towards the source of cAMP. Note that distinct elements of the motion pattern described before, such as the polarity-induced transitions in the position of the cargo with respect to the cell, are also visible in the presence of a chemical gradient. This suggests that key features of the cell-cargo dynamics in the absence of chemical cues are preserved during chemotactic motion, indicating that our present results provide a promising starting point for a more detailed study of directional microtransport in chemical gradients.

VII. CONCLUSION AND OUTLOOK

In this study, we highlight the potential of motile amoeboid cells to act as autonomous carriers of micron-sized cargo and investigate the transport dynamics of this active biohybrid system. Our experiments reveal a complex cell-cargo motion pattern involving recurrent phases of polar displacement that alternate with an isotropic resting state. This can be qualitatively explained based on the mechanoresponsiveness of amoeboid cells: their crawling motility relies on cyclic cell shape changes to pull the cell body forward, a process that is governed by surface adhesion in conjunction with the mechanical stresses generated by the cell's cytoskeletal machinery [49–51]. The geometry of the surrounding environment, such as the presence of a cargo, thus strongly affects cell polarity and, consequently, migration patterns [52–56]. In our specific case, the cell is positioned in a confined space

between the coverslip and cargo surfaces, where the latter provides an additional substrate for adhesion compared to a cell without cargo. This may explain the spontaneous bursts of cell polarity observed in our experiments, as adhesion to the cargo triggers additional actin activity, which in turn induces cytoskeletal symmetry breaking, thus promoting motility along the direction of the cell-cargo axis. The characteristic lifetime of cell polarity $\tau_p = \sigma^{-1}$ results in persistent motion [52,57,58]. As a consequence, the cell pulls the cargo forward, resulting in a net displacement during these motile phases. In short, confinement-induced cell-cargo interactions determine the transport capacities as a whole. We therefore envision that different cargo shapes and sizes may significantly impact the cytoskeletal activity and polarization dynamics, allowing for a dedicated design of the transport properties of active biohybrids in the future.

The active particle model that we develop here connects the experimentally observed cell-cargo dynamics at the level of the individual cellular truck with the long-time displacement of the biohybrid system as a whole, thereby enabling us to assess the relevant timescales and to predict the effective transport properties, quantified in terms of the mean-square displacement of colloids and, in particular, the effective long-time diffusion coefficient. The theoretical analysis unveils how the diffusivity is determined by the interplay between the intrinsic persistence of cell polarity and characteristic time scales of the cell-cargo interaction, such as the polarization rate. Notably, we predict that an optimal cargo size enhances the diffusivity of cellular trucks, such that loaded cells may even outperform unloaded ones in terms of their long-time transport capacity.

The data that support the plots within this paper and other findings of this study are available from the corresponding author upon request.

ACKNOWLEDGMENTS

V.L., S.K., R.L., and C.B. acknowledge financial support via the IMPRS *Multiscale Bio-Systems*, S.S.P. and C.B. thank the Deutsche Forschungsgemeinschaft (DFG) for funding (Sachbeihilfe BE 3978/3-3). We thank Kirsten Sachse and Maïke Stange for technical support and Fernando Peruani for valuable comments on the manuscript.

V.L. performed experimental research, V.L. and R.G. analyzed data and designed the model, R.G. performed analytical derivations and mathematical analysis, O.N. and S.S.P. contributed experimental data, V.L., R.G., and C.B. wrote the manuscript, S.K. and R.L. cosupervised the project, and C.B. designed the research and supervised the project.

The authors declare no competing interests.

APPENDIX: METHODS

1. Cell culturing

LimE-mRFP MyoII-GFP expressing AX2 *D. discoideum* cells (kindly provided by Günther Gerisch, Martinsried) are adherently grown on the bottom surface of tissue culture flasks (TC Flask T75 Standard, Sarstedt AG & Co. KG, Nümbrecht, Germany), cultured at 22 °C in nutrient medium (HL5 medium including glucose, Formedium Ltd., Norfolk, England) supplemented with a penicillin (final concentration: 100 I.U./ml) and streptomycin (final concentration: 100 µg/ml) antibiotics mix (CELLPURE® Pen/Strep-PreMix, Carl Roth GmbH+Co. KG, Karlsruhe, Germany). In addition, G418 (G418 disulfate ultrapure, VWR International, LLC) and Blasticidin [Blasticidin S (hydrochloride), CAYMAN CHEMICAL, Ann Arbor, Michigan, USA] are added as selection agents, in each case to a final concentration of 10 µg/ml. To avoid confluency, cells are subcultured into new flasks every two days via 1:20 dilution of a cell suspension from a previous flask, or 1:64 prior to weekends. Cell cultures are renewed every four weeks to avoid accumulation of any undesired mutation eventually arising by genetic drift. In addition, we also use LifeAct-mRFP expressing AX2 *D. discoideum* cells (kindly provided by Maja Marinowic and Igor Weger, Zagreb), which are cultivated analogously, the only difference being the use of just one selection agent (G418).

2. Sample preparation

Polystyrene spherical microparticles [Polybead® Microspheres, Polysciences Europe GmbH, Hirschberg an der Bergstrasse, Germany and Polystyrene particles (PS-R), microParticles GmbH, Berlin, Germany] are suspended in phosphate buffer (Sørensen buffer: in deionized water, 2 g l⁻¹ KH₂PO₄, 0.36 g l⁻¹ Na₂HPO₄, 50 µl l⁻¹ 1M MgCl₂, 50 µl l⁻¹ 1M CaCl₂; pH 6.0) to have a particle number density of 5 × 10⁵ ml⁻¹.

Cells are harvested from a flask, normally during the subculturing procedure, always far from confluency. The obtained cell suspension is then diluted to obtain a cell count of roughly 50 × 10³ ml⁻¹, thus 2 ml of the new suspension are put into a culture dish (FluoroDish™ tissue culture dish—35 mm diameter, 23 mm well, World Precision Instruments, Inc., Sarasota, Florida, USA). The sample is left settling for 15 min to let cells sediment and adhere on the bottom of a dish; afterwards, 50 µl of particle suspension are added while gently shaking the dish in order to achieve a more uniform particle distribution on the substrate.

For chemotaxis experiments, Lifeact-mRFP AX2 expressing *D. discoideum* cells are washed and starved in a phosphate buffer (including 14.6 mM KH₂PO₄ and 2 mM Na₂HPO₄; Merck KGaA, Darmstadt, Germany) for 3–4 h prior to the experiments. To establish a linear

gradient of chemoattractant, ibidi μ -Slide Chemotaxis chambers (ibidi GmbH, Martinsried, Germany) are used. The gradient is formed by diffusion between two reservoirs that are separated by a channel (width of 1 mm). One reservoir is filled with a mixture of particles and cells (ratio 1:100) in buffer and the second reservoir with 5 mM cAMP. The sample is imaged at a frame rate of two frames per minute for up to 6 h.

3. Imaging

The sample is imaged in time lapse by means of multichannel confocal imaging using a laser scanning microscope (LSM 780, Zeiss, Oberkochen, Germany). A DPSS laser, generating 561 nm electromagnetic radiation, excites the fluorophore mRFP colocalizing with F -actin, whose emission is bandpass filtered (582–754 nm) and then detected by a photomultiplier. An argon-ion laser, emitting at the wavelength 488 nm, is used to excite the fluorophore GFP colocalizing with myosin II; again, the fluorescence emission is bandpass filtered (493–556 nm) before detection. All the transmitted light is collected by a third acquisition channel, used for particle imaging, where images arise from the contrast generated by discontinuities of the refractive index.

The focal plane is set to be in correspondence with the substrate surface to focus the ventral surface of cells together with a bottom section of the particle. The depth of field is roughly 0.7 μm to 0.8 μm (detector pinhole aperture of 1 Airy Units, $63\times/40\times$ objective), enabling us to collect light from an optimal volume of the cell body, granting good signal-to-noise ratio at low laser intensities without excessively compromising the resolution of the optical sectioning. For any detected cell-particle system, images are recorded every 10 s, until the system of interest leaves the field of view or becomes unsuitable (due to cell division or other cells and particles altering the configuration of the system), for a maximum time of 1 h.

4. Image analysis

The image processing and data analysis is performed using custom algorithms written as MATLAB[®] code.

Cell segmentation relies on the 561-nm-source fluorescence channel, exploiting the contrast created by the fluorescence emission from the mRFP labeling the F -actin, while particle segmentation is based on bright-field images from the transmitted light channel. For both objects, images first undergo median filtering, followed by a contrast enhancement protocol, involving a sequence of non-linear histogram remapping steps. The processed images are then binarized with a threshold determined by Otsu's method [59] and the segmented objects are tracked through the frames. In the case of cells, boundaries detected from segmentation are further processed with an active contouring algorithm [60]. The two-dimensional position vectors

\mathbf{r} and \mathbf{R} for the cell and cargo, respectively, defined in the focal plane parallel to the substrate surface, are defined as the centroids of the objects identified by binarization.

5. Data analysis

To compensate for the cell-to-cell variability in size—the cell size sets the spatial scale of relative motion of the cell and cargo and, thus, affects relative distance distributions—the cell-cargo distance $l(t) = |\mathbf{R} - \mathbf{r}|$ is rescaled by an effective cell radius r_c , which is determined to match the average projected cell area $\langle A_c \rangle = \pi r_c^2$, prior to the calculation of the population-averaged histograms of the cell-cargo distance as shown in Fig. 3.

For the experimental estimation of the polarization rate λ , detection of polarization events is performed as follows. First, the time series $l(t) = |\mathbf{R}(t) - \mathbf{r}(t)|$ of the cell-cargo distance is renormalized by subtracting the time-averaged mean $\overline{l(t)}$ and subsequent division by the standard deviation in each recording. Population-averaged histograms of all observations reveal a peaked, asymmetric distribution, comparable to Fig. 4(b), which is well approximated by the sum of two Gaussian distributions. The main contribution of the histogram stems from resting and motile phases, where $l(t)$ fluctuates around a preferred value l_0 ; the asymmetry stems from transitions during which the distance $l(t)$ becomes small. The inspection of all histograms suggests that fluctuations of the distance $l(t)$ towards zero by more than 1.75 standard deviations from its mean value indicates a transition and therefore provides a reliable cutoff criterion. Based on this cutoff, the time series is binarized and transitions are counted. The estimation of the polarization rate λ from the detected events is based on the assumption that the polarization process is Poissonian. Accordingly, the probability of observing k polarization events in a time interval τ is given by the Poisson distribution

$$P_\tau(k|\lambda) = \frac{(\lambda\tau)^k e^{-\lambda\tau}}{k!}, \quad (\text{A1})$$

implying the likelihood

$$\mathcal{L} = \prod_{i=1}^N P_{\tau_i}(k_i|\lambda). \quad (\text{A2})$$

For each colloid size, we observe $N = 10$ independent experimental realizations of length τ_i and count the number of polarization events k_i ($i = 1, 2, \dots, N$). The maximum likelihood estimator $\hat{\lambda}$ for rate λ is determined by the total number of observed events divided by the total observation time:

$$\hat{\lambda} = \frac{\sum_{i=1}^N k_i}{\sum_{j=1}^N \tau_j}. \quad (\text{A3})$$

In the vicinity of its maximum value, we approximate the likelihood as a Gaussian distribution with mean $\hat{\lambda}$ and standard deviation

$$\sigma_{\lambda} = \frac{\hat{\lambda}}{\sqrt{\sum_{j=1}^N k_j}}. \quad (\text{A4})$$

In Fig. 5(a), the error bars graphically represent this 1σ interval. This automatic transition counting yields consistent results with manual counting of transitions that is based on the binarizing and thresholding of recurrence plots of the distance $l(t)$ via Otsu's method, where such events appear as distinct horizontal and vertical lines.

The temporal dependence of the mean-squared displacement of colloids, as shown in Fig. 1(b), is estimated as follows. At first, the time-averaged mean-squared displacement

$$\delta_{\mu}(m\Delta) = \frac{1}{n_{\mu} - m} \sum_{k=1}^{n_{\mu}-m} |\mathbf{R}_{\mu}(t_{k+m}) - \mathbf{R}_{\mu}(t_k)|^2 \quad (\text{A5})$$

is calculated for each trajectory, where $\mathbf{R}_{\mu}(t_k)$ denotes the position of colloid μ in frame k , n_{μ} is the total number of frames in the μ th trajectory, and Δ is the time step of image acquisition (inverse frame rate). We assume that the colloid displacements are Gaussian distributed with zero mean in two dimensions,

$$\bar{P}(\mathbf{R} - \mathbf{R}_0) = \frac{1}{\pi l_2} \exp\left(-\frac{|\mathbf{R} - \mathbf{R}_0|^2}{l_2}\right), \quad (\text{A6})$$

which is justified at least for long time intervals. The aim is to estimate the width of this Gaussian distribution as a function of the lag parameter m that is the ensemble-averaged mean-square displacement l_2 . Given that the measured colloid displacements are Gaussian and independent, the time-averaged mean-squared displacement $\delta_{\mu}(m\Delta)$ of a single trajectory follows a Gamma distribution,

$$p(\delta) = \frac{\delta^{\alpha-1}}{\Gamma(\alpha)} \beta^{\alpha} e^{-\beta\delta} \quad (\text{A7})$$

with shape parameter $\alpha = n_{\mu} - m$ and inverse scale parameter $\beta = (n_{\mu} - m)/l_2$. From this distribution, we construct a likelihood for the observed displacements, given the parameter l_2 to be estimated as a function of the time lag $m\Delta$. For small time lags—if the time lag is shorter than the shortest trajectory—the maximum likelihood estimator for the ensemble-averaged mean-squared displacements equals the weighted average of the time-averaged

mean-squared displacements of all trajectories,

$$l_2(m\Delta) = \frac{\sum_{\mu=1}^N (n_{\mu} - m) \delta_{\mu}(m\Delta)}{\sum_{\nu=1}^N (n_{\nu} - m)}, \quad (\text{A8})$$

where the weights correspond to the number of terms in the sum of Eq. (A5), i.e., the number of displacements they are calculated from, and N is the total number of tracks. As the time lag increases, it may become larger than the number of frames in short tracks and, consequently, Eq. (A8) loses its applicability. In that case, we construct the likelihood as the product

$$\mathcal{L} = \left[\prod_{\mu=1}^{N_c} p(\delta_{\mu}(m\Delta)) \right] \left[\prod_{\nu=1}^{N_i} P(\delta_{\nu}(n_{\nu}\Delta)) \right], \quad (\text{A9})$$

where the first product runs over the N_c trajectories that contain more than m frames and the second product includes those N_i tracks that have less than or equal to m frames ($N = N_c + N_i$). In the second product,

$$P(\delta) = \int_{\delta}^{\infty} d\delta' p(\delta') \quad (\text{A10})$$

is the probability that the time-averaged mean-squared displacement is larger than δ . In this way, the fact that the corresponding colloid is observed to displace by at least $\delta_{\mu}(n_{\mu}\Delta)$ for large time lags is taken into account. This construction of the likelihood is based on the assumption that the mean-squared displacement is a nondecreasing function in the long-time limit. We eventually maximize the likelihood [Eq. (A9)] numerically to obtain an estimator for l_2 .

6. Theoretical estimation of the diffusion coefficient

In order to assess how the long-time transport properties of the cell-cargo truck depend on the parameter values, we derive the long-time limit analytically. For this purpose, the cell-cargo model dynamics is simplified as follows: (i) in the isotropic state, the cell undergoes Brownian diffusion while the cargo is located at a fixed distance from the cell, performing random motion around it; (ii) in the polarized state, the cell performs a persistent random walk with a fixed speed v_0 and a finite persistence length parametrized by the angular noise strength D_{φ} , carrying the cargo on its back; (iii) transition phases—polarity bursts during which the cell pulls the cargo from the leading to the trailing edge—are fast processes compared to other relevant timescales and are therefore assumed to occur instantaneously. This corresponds, formally, to the limit $\alpha \rightarrow \infty$, implying that we neglect the timescale of the relative dynamics of the cell and cargo. The simplified model is formally represented by two coupled master equations. We perform an expansion in Fourier modes. Only

one Fourier coefficient, corresponding to the density of cellular trucks $\rho(\mathbf{r}, t)$ at position \mathbf{r} at time t , is a slow variable (conserved quantity) that dominates the long-time dynamics. Therefore, the coupled system of Fourier modes can be systematically reduced onto the density by adiabatic elimination of fast modes. To lowest order in spatial gradients, the diffusion equation is obtained, from which the diffusion constant \mathcal{D} can be read off. Mathematical details of the calculation are provided as Supplemental Material [42]; see also Ref. [61] where similar methods were applied for coarse graining.

The abovementioned simplified model overestimates the actual diffusion coefficient as changes of the cargo position during polarity bursts of the cell are not instantaneous. During polarity bursts, during which the cell and particle interchange their positions, little net displacement of the cellular truck as such occurs. We develop a heuristic correction based on the idea that a run of the cell can be subdivided into two phases: first, the polarized cell crawls underneath the particle and pulls it onto its back and, second, it moves persistently with the cell on its back (motile phase); cf. Fig. 1. We assume that no active transport occurs as the cell and cargo change their relative positions. Accordingly, the actual time spent in the persistent run phase is decreased. This leads to a correction factor $\alpha/(\alpha + \lambda)$ of the diffusion coefficient that equals the probability of not being in the resting phase.

-
- [1] M. Sitti, H. Ceylan, W. Hu, J. Giltinan, M. Turan, S. Yim, and E. Diller, Biomedical applications of untethered mobile milli/microrobots, *Proc. IEEE* **103**, 205 (2015).
- [2] D. Xu, Y. Wang, C. Liang, Y. You, S. Sanchez, and X. Ma, Self-propelled micro/nanomotors for on-demand biomedical cargo transportation, *Small* **16**, 1902464 (2020).
- [3] H. Bayley and P. S. Cremer, Stochastic sensors inspired by biology, *Nature* **413**, 226 (2001).
- [4] S. Sánchez and M. Pumera, Nanorobots: The ultimate wireless self-propelled sensing and actuating devices, *Chem. Asian J.* **4**, 1402 (2009).
- [5] T. Patino, R. Mestre, and S. Sánchez, Miniaturized soft bio-hybrid robotics: A step forward into healthcare applications, *Lab Chip* **16**, 3626 (2016).
- [6] M. Paoluzzi, R. Di Leonardo, M. C. Marchetti, and L. Angelani, Shape and displacement fluctuations in soft vesicles filled by active particles, *Sci. Rep.* **6**, 34146 (2016).
- [7] A. Joseph, C. Contini, D. Cecchin, S. Nyberg, L. Ruiz-Perez, J. Gaitzsch, G. Fullstone, X. Tian, J. Azizi, J. Preston, G. Volpe, and G. Battaglia, Chemotactic synthetic vesicles: Design and applications in blood-brain barrier crossing, *Sci. Adv.* **3**, e1700362 (2017).
- [8] H. Hess and J. L. Ross, Non-equilibrium assembly of microtubules: from molecules to autonomous chemical robots, *Chem. Soc. Rev.* **46**, 5570 (2017).
- [9] L. Tang, Y. Zheng, M. B. Melo, L. Mabardi, A. P. Castaño, Y.-Q. Xie, N. Li, S. B. Kudchodkar, H. C. Wong, E. K. Jeng, M. V. Maus, and D. J. Irvine, Enhancing T cell therapy through TCR-signaling-responsive nanoparticle drug delivery, *Nat. Biotechnol.* **36**, 707 (2018).
- [10] F. Soto, J. Wang, R. Ahmed, and U. Demirci, Medical micro/nanorobots in precision medicine, *Adv. Sci.* **7**, 2002203 (2020).
- [11] M. Sitti, Voyage of the microrobots, *Nature* **458**, 1121 (2009).
- [12] R. W. Carlsen and M. Sitti, Bio-hybrid cell-based actuators for microsystems, *Small* **10**, 3831 (2014).
- [13] L. K. Abdelmohsen, F. Peng, Y. Tu, and D. A. Wilson, Micro- and nano-motors for biomedical applications, *J. Mater. Chem. B* **2**, 2395 (2014).
- [14] W. Wang, W. Duan, S. Ahmed, T. E. Mallouk, and A. Sen, Small power: Autonomous nano- and micromotors propelled by self-generated gradients, *Nano Today* **8**, 531 (2013).
- [15] G. Hwang, R. Braive, L. Couraud, A. Cavanna, O. Abdelkarim, I. Robert-Philip, A. Beveratos, I. Sagnes, S. Haliyo, and S. Régner, Electro-osmotic propulsion of helical nanobelt swimmers, *Int. J. Robot. Res.* **30**, 806 (2011).
- [16] L. Ricotti, B. Trimmer, A. W. Feinberg, R. Raman, K. K. Parker, R. Bashir, M. Sitti, S. Martel, P. Dario, and A. Menciassi, Biohybrid actuators for robotics: A review of devices actuated by living cells, *Sci. Robot.* **2**, eaaq0495 (2017).
- [17] I. C. Yasa, H. Ceylan, U. Bozuyuk, A.-M. Wild, and M. Sitti, Elucidating the interaction dynamics between microswimmer body and immune system for medical microrobots, *Sci. Robot.* **5**, eaaz3867 (2020).
- [18] J. Zhang, F. Mou, Z. Wu, J. Song, J. E. Kauffman, A. Sen, and J. Guan, Cooperative transport by flocking phototactic micromotors, *Nanoscale Adv.* **3**, 6157 (2021).
- [19] Y. Alapan, O. Yasa, B. Yigit, I. C. Yasa, P. Erkoç, and M. Sitti, Microrobotics and microorganisms: Biohybrid autonomous cellular robots, *Annu. Rev. Control Robot. Auton. Syst.* **2**, 205 (2019).
- [20] L. Sun, Y. Yu, Z. Chen, F. Bian, F. Ye, L. Sun, and Y. Zhao, Biohybrid robotics with living cell actuation, *Chem. Soc. Rev.* **49**, 4043 (2020).
- [21] M. Pacheco, B. J. Sánchez, and A. Escarpa, Functional coatings enable navigation of light-propelled micromotors in blood for effective biodegradation, *Nanoscale* **13**, 17106 (2021).
- [22] P. Friedl and B. Weigelin, Interstitial leukocyte migration and immune function, *Nat. Immunol.* **9**, 960 (2008).
- [23] K. Wolf, R. Müller, S. Borgmann, E. Bröcker, and P. Friedl, Amoeboid shape change and contact guidance: T-lymphocyte crawling through fibrillar collagen is independent of matrix remodeling by MMPs and other proteases, *Blood* **102**, 3262 (2003).
- [24] M. A. Titus and H. V. Goodson, An evolutionary perspective on cell migration: Digging for the roots of amoeboid motility, *J. Cell Bio.* **216**, 1509 (2017).
- [25] A. C. Anselmo, J. B. Gilbert, S. Kumar, V. Gupta, R. E. Cohen, M. F. Rubner, and S. Mitragotri, Monocyte-mediated delivery of polymeric backpacks to inflamed tissues: A generalized strategy to deliver drugs to treat inflammation, *J. Controlled Release* **199**, 29 (2015).
- [26] J. Shao, M. Xuan, H. Zhang, X. Lin, Z. Wu, and Q. He, Chemotaxis-guided hybrid neutrophil micromotors for targeted drug transport, *Angew. Chem. Int. Ed.* **56**, 12935 (2017).

- [27] J. Xue, Z. Zhao, L. Zhang, L. Xue, S. Shen, Y. Wen, Z. Wei, L. Wang, L. Kong, H. Sun, Q. Ping, R. Mo, and C. Zhang, Neutrophil-mediated anticancer drug delivery for suppression of postoperative malignant glioma recurrence, *Nat. Nanotechnol.* **12**, 692 (2017).
- [28] M. C. Marchetti, J. F. Joanny, S. Ramaswamy, T. B. Liverpool, J. Prost, M. Rao, and R. A. Simha, Hydrodynamics of soft active matter, *Rev. Mod. Phys.* **85**, 1143 (2013).
- [29] H. Chaté, Dry aligning dilute active matter, *Annu. Rev. Condens. Matter Phys.* **11**, 189 (2020).
- [30] M. Bär, R. Großmann, S. Heidenreich, and F. Peruani, Self-propelled rods: Insights and perspectives for active matter, *Annu. Rev. Condens. Matter Phys.* **11**, 441 (2020).
- [31] T. Vicsek, A. Czirók, E. Ben-Jacob, I. Cohen, and O. Shochet, Novel Type of Phase Transition in a System of Self-Driven Particles, *Phys. Rev. Lett.* **75**, 1226 (1995).
- [32] J. Toner and Y. Tu, Long-Range Order in a Two-Dimensional Dynamical XY Model: How Birds Fly Together, *Phys. Rev. Lett.* **75**, 4326 (1995).
- [33] L. Huber, R. Suzuki, T. Krüger, E. Frey, and A. R. Bausch, Emergence of coexisting ordered states in active matter systems, *Science* **361**, 255 (2018).
- [34] M. Grognot and K. M. Taute, More than propellers: How flagella shape bacterial motility behaviors, *Curr. Opin. Microbiol.* **61**, 73 (2021).
- [35] T. Vicsek and A. Zafeiris, Collective motion, *Phys. Rep.* **517**, 71 (2012).
- [36] H. D. Vuijk, H. Merlitz, M. Lang, A. Sharma, and J.-U. Sommer, Chemotaxis of Cargo-Carrying Self-Propelled Particles, *Phys. Rev. Lett.* **126**, 208102 (2021).
- [37] C. Jin, Y. Chen, C. C. Maass, and A. J. T. M. Mathijssen, Collective Entrainment and Confinement Amplify Transport by Schooling Microswimmers, *Phys. Rev. Lett.* **127**, 088006 (2021).
- [38] P. Friedl, S. Borgmann, and E.-B. Bröcker, Amoeboid leukocyte crawling through extracellular matrix: Lessons from the *Dictyostelium* paradigm of cell movement, *J. Leukoc. Biol.* **70**, 491 (2001).
- [39] Y. Artemenko, T. J. Lampert, and P. N. Devreotes, Moving towards a paradigm: Common mechanisms of chemotactic signaling in *Dictyostelium* and mammalian leukocytes, *Cell. Mol. Life Sci.* **71**, 3711 (2014).
- [40] W. F. Loomis, D. Fuller, E. Gutierrez, A. Groisman, and W.-J. Rappel, Innate non-specific cell substratum adhesion, *PLoS ONE* **7**, e42033 (2012).
- [41] O. Nagel, M. Frey, M. Gerhardt, and C. Beta, Harnessing motile amoeboid cells as trucks for microtransport and-assembly, *Adv. Sci.* **6**, 1801242 (2019).
- [42] See Supplemental Material at <http://link.aps.org/supplemental/10.1103/PhysRevApplied.18.034014> for a description of movies and complementary technical details, which includes Ref. [61].
- [43] W.-J. Rappel and L. Edelstein-Keshet, Mechanisms of cell polarization, *Curr. Opin. Syst. Biol.* **3**, 43 (2017).
- [44] J. Dalous, E. Burghardt, A. Müller-Taubenberger, F. Bruckert, G. Gerisch, and T. Bretschneider, Reversal of cell polarity and actin-myosin cytoskeleton reorganization under mechanical and chemical stimulation, *Biophys. J.* **94**, 1063 (2008).
- [45] J.-P. Eckmann, S. O. Kamphorst, and D. Ruelle, Recurrence plots of dynamical systems, *Europhys. Lett.* **4**, 973 (1987).
- [46] N. Marwan, M. C. Romano, M. Thiel, and J. Kurths, Recurrence plots for the analysis of complex systems, *Phys. Rep.* **438**, 237 (2007).
- [47] A. C. Coughlan and M. A. Bevan, Effective colloidal interactions in rotating magnetic fields, *J. Chem. Phys.* **147**, 074903 (2017).
- [48] C. Gardiner, *Stochastic Methods: A Handbook for the Natural and Social Sciences*, Springer Series in Synergetics (Springer, 2009).
- [49] R. Ananthakrishnan and A. Ehrlicher, The forces behind cell movement, *Int. J. Biol. Sci.* **3**, 303 (2007).
- [50] B. Álvarez-González, R. Meili, E. Bastounis, R. A. Firtel, J. C. Lasheras, and J. C. del Álamo, Three-dimensional balance of cortical tension and axial contractility enables fast amoeboid migration, *Biophys. J.* **108**, 821 (2015).
- [51] C. A. Copos, S. Walcott, J. C. del Álamo, E. Bastounis, A. Mogilner, and R. D. Guy, Mechanosensitive adhesion explains stepping motility in amoeboid cells, *Biophys. J.* **112**, 2672 (2017).
- [52] R. J. Petrie, A. D. Doyle, and K. M. Yamada, Random versus directionally persistent cell migration, *Nat. Rev. Mol. Cell Biol.* **10**, 538 (2009).
- [53] O. Nagel, C. Guven, M. Theves, M. Driscoll, W. Losert, and C. Beta, Geometry-driven polarity in motile amoeboid cells, *PLoS ONE* **9**, e113382 (2014).
- [54] A. D. Doyle, F. W. Wang, K. Matsumoto, and K. M. Yamada, One-dimensional topography underlies three-dimensional fibrillar cell migration, *J. Cell Biol.* **184**, 481 (2009).
- [55] L. Boneschansker, J. Yan, E. Wong, D. M. Briscoe, and D. Irimia, Microfluidic platform for the quantitative analysis of leukocyte migration signatures, *Nat. Commun.* **5**, 4787 (2014).
- [56] L. Pieuchot, J. Marteau, A. Guignandon, T. Dos Santos, I. Brigaud, P.-F. Chauvy, T. Cloatre, A. Ponche, T. Petithory, P. Rougerie, M. Vassaux, J.-L. Milan, N. T. Wakhloo, A. Spangenberg, M. Bigerelle, and K. Anselme, Curvotaxis directs cell migration through cell-scale curvature landscapes, *Nat. Commun.* **9**, 3995 (2018).
- [57] R. Gorelik and A. Gautreau, Quantitative and unbiased analysis of directional persistence in cell migration, *Nat. Protoc.* **9**, 1931 (2014).
- [58] H. V. Prentice-Mott, Y. Meroz, A. Carlson, M. A. Levine, M. W. Davidson, D. Irimia, G. T. Charras, L. Mahadevan, and J. V. Shah, Directional memory arises from long-lived cytoskeletal asymmetries in polarized chemotactic cells, *Proc. Natl. Acad. Sci. USA* **113**, 1267 (2016).
- [59] N. Otsu, A threshold selection method from gray-level histograms, *IEEE Trans. Syst. Man. Cybern.* **9**, 62 (1979).
- [60] C. Xu and J. L. Prince, Snakes, shapes, and gradient vector flow, *IEEE Trans. Image Process.* **7**, 359 (1998).
- [61] L. Gómez, R. Großmann, and F. Peruani, Markovian robots: Minimal navigation strategies for active particles, *Phys. Rev. E* **97**, 042604 (2018).